Chinese Chemical Letters 35 (2024) 108484

Contents lists available at ScienceDirect

Chinese Chemical Letters

journal homepage: www.elsevier.com/locate/cclet

Core-shell heterostructure by coupling layered ReS_2 with Co_9S_8 nanocubes for boosted oxygen evolution reaction

Xu Yu[a,*], Zhiqiang Pan[a], Chengang Pei[b], Longjie Lin[a], Yanhui Lu[a], Ho Seok Park[b], Huan Pang[a,*]

[a] School of Chemistry and Chemical Engineering, Yangzhou University, Yangzhou 225009, China
[b] School of Chemical Engineering, Sungkyunkwan University, 2066, Seobu-ro, Jangan-gu, Suwon-si, Gyeonggi-do 440-746, Republic of Korea

ARTICLE INFO

Article history:
Received 16 March 2023
Revised 8 April 2023
Accepted 19 April 2023
Available online 21 April 2023

Keywords:
Oxygen evolution reaction
Rhenium disulfide
Metal-organic framework
Heterostructure
Core-shell

ABSTRACT

The controllable morphology and composition of catalysts are crucial to improving the electrocatalytic activity of oxygen evolution reaction (OER). Herein, we construct a bimetallic heterostructure by sulfidation and hydrothermal methods, and the layered ReS_2 is vertically aligned on Prussian blue-derived hollow Co_9S_8 nanocubes (Co_9S_8@ReS_2). The core-shell structure of Co_9S_8@ReS_2 can effectively prevent the restacking of layered ReS_2, expose the abundant surface area and improve the utilization of electrocatalytic sites, resulting in fast electrolyte diffusion and charge transfer during OER. Due to the synergistic effect of the core-shell morphology and the formed bimetallic heterostructure, Co_9S_8@ReS_2 exhibits excellent catalytic OER performance. At 10 mA/cm^2, only 288 mV of overpotential is required with the Tafel slope of 73.3 mV/dec for Co_9S_8@ReS_2, which are both lower than that of Co_9S_8 and ReS_2. Meanwhile, Co_9S_8@ReS_2 exhibits high catalytic stability and low charge transfer resistance and the boosted active sites are confirmed by density functional theory. This work provides a rational design of the OER catalysts by constructing the bimetallic heterostructure.

Developing clean and renewable energy is the future of a green economy, which can alleviate the stress of environmental pollution from the excessive combustion of fossil fuels [1–4]. Sustainable and high-efficiency alternatives to fossil fuels are imminent for realizing a sustainable society. Hydrogen production by electrocatalytic water splitting is acknowledged as a promising route for renewable energy with zero environmental emissions [5–9]. Oxygen evolution reaction (OER) is a complicated four-electron transfer process of electrocatalytic water splitting, and the slow sluggish kinetics is still a critical issue to be solved [10–12]. The noble metal-based catalysts own excellent catalytic OER performance like low overpotential and fast kinetics behavior [13–15], but the high price and resource scarcity slow down their commercialization [16–18]. Therefore, it is urgent to develop cheap and efficient catalysts to satisfy the requirement of practical applications.

Transition metal-based catalysts (oxides, sulfides, phosphides) with the merits of abundant reserves and competitive cost have attracted attention. Among them, transition metal sulfides (TMS), such as FeS [19,20], Co_3S_4 [21,22] and Ni_3S_2 [23,24], have been demonstrated to show excellent catalytic activity in alkaline electrolytes and considered the prospective candidates for OER. Prussian blue (PB) is a member of metal-organic frameworks, which has the advantage of a controllable morphological structure and chemical composition. TMS catalysts derived from PBA can maintain the nanocubic structure, which has been proven to be precursors or templates for preparing multifarious forms of nanomaterials [25–27], such as $Fe_5Ni_4S_8$/NiS with porous carbon layer [28] and Co_3S_4@MoS_2 hetero-structured catalyst [29]. Specifically, the hollow structure derived from PB has attracted much attention because of its abundant active sites, rapid charge transfer, and short electrolyte diffusion pathway [30–32]. In addition to the controllable structure effect, it is anticipated to develop an effective TMS-based catalyst for enhanced OER activity by introducing a second functional component.

Rhenium disulfide (ReS_2), as a member of two-dimensional transition metal dichalcogenides (TMDs), owns a distorted and thermodynamically stable 1T crystal structure, which induces the strong electronic decoupling and unique chemical/physical properties [33–35]. The catalytic activity of ReS_2 mainly results from the edge sites, but the basal planes have poor catalytic activity [36–38]. The expanded interlayer space can expose more potential active sites [39,40]. Numerous studies have been reported to construct the controllable composition of ReS_2-based catalysts

---

* Corresponding authors.
E-mail addresses: yxypz15@yzu.edu.cn (X. Yu), panghuan@yzu.edu.cn (H. Pang).

https://doi.org/10.1016/j.cclet.2023.108484

by atomic doping for oxygen evolution reaction [41,42]. Despite it, the adjusted morphological structure is also important to affect the electrocatalytic activity of catalysts. Recently, the core-shell structured catalysts with this particular property have attracted attention, which results from the synergistic effect of core and shell properties [43–45]. Meanwhile, the core-shell structure can effectively hinder the aggregation of layered materials, expose more active sites and promote ion diffusion and charge transfer, such as core-shell Cu@Fe@Ni metallic aerogel [46] and core-shell $FeS_2@NiS_2$ [47]. In comparison to the single component, the electrocatalysts with the core-shell structure are greatly important to improve the chemical catalysis due to the synergistic efficiency of two different components. The PBA-derived metal sulfides with the nanosized structure are easy to agglomerate due to their 'Ostwald ripening' mechanism by their high surface energy. The construction of a core-shell structure by encapsulating the nanostructures with TMDs is a rational design to counteract this issue.

Herein, the couple of layered ReS_2 and hollow Co_9S_8 nanocubes ($Co_9S_8@ReS_2$) with a core-shell structure were constructed by the combination of co-precipitation and two-step temperature-raising hydrothermal methods. The strong interfacial coupling is caused by the inner Co_9S_8 core and outer ReS_2 shell, which all benefit its electrocatalytic activity in 1 mol/L KOH. Moreover, $Co_9S_8@ReS_2$ requires a lower overpotential, smaller Tafel slope and charge transfer resistance than the control samples. The small Tafel slope and low charge transfer resistance imply the fast kinetic behavior of $Co_9S_8@ReS_2$. This work is instructive to design hollow materials with core-shell structures as an effective catalyst for water splitting.

Fig. 1a illustrates the synthetic procedure for the preparation of core-shell structure. Firstly, the cobalt-iron Prussian blue analogy (CoFe PBA) is obtained by the co-precipitation method. After the sulfidation treatment by hydrothermal method at 120 °C, Co_9S_8 nanocubes are formed through the ionic exchange reaction between $[Fe(CN)_6]^{3-}$ and S^{2-}. Furthermore, the ruthenium sulfides (ReS_2) are grown on the surface of Co_9S_8 nanocubes at 240 °C, and the hybrid is thermally activated at 350 °C for 2 h to finally obtain the core-shell $Co_9S_8@ReS_2$ heterostructure with high crystallinity.

The morphological structure of $Co_9S_8@ReS_2$ was initially characterized by scanning electron microscopy (SEM). CoFe PBA shows a well-defined nanocubic structure (Fig. S1a in Supporting information). The nanocubic structure collapsed and the surface becomes rough for Co_9S_8 due to the sulfidation treatment (Fig. S1c in Supporting information). As shown in Fig. 1b, ReS_2 nanosheets are vertically aligned on the Co_9S_8 surface for $Co_9S_8@ReS_2$, and the edge of ReS_2 nanosheets are cross-connected with each other. The structure was further confirmed by Transmission electron microscopy (TEM), which is well-matched with the SEM analysis. CoFe PBA shows a smooth surface and the average size of the nanocube is about 200 nm (Fig. S1b in Supporting information). The rough surface can be found for Co_9S_8 in Fig. S1d (Supporting information), and the average size of the nanocubes is about 150 nm due to the collapsed surface by sulfidation. The obtained ReS_2 nanosheets by hydrothermal method show a serious agglomeration (Fig. S2 in Supporting information). The core-shell morphology can be found for $Co_9S_8@ReS_2$ in Figs. 1c and d, and the hollow structure is constructed by inner Co_9S_8 nanocubes and outer ReS_2 nanosheets. Fig. 1e shows the distinct lattice fringes, and the interplanar spacing of 0.61 and 0.29 nm correspond to the (002) plane of ReS_2 and (311) plane of Co_9S_8, respectively. The elemental mapping result is shown in Fig. 1f, revealing the uniform distribution of Re, Co, S and O elements are uniformly distributed on $Co_9S_8@ReS_2$, and the O elements probably are derived from the unavoidable surface oxidation of the samples in the air. Meanwhile, the outline of the distributed Re elements is much larger than that of Co elements confirming the core-shell structure of $Co_9S_8@ReS_2$.

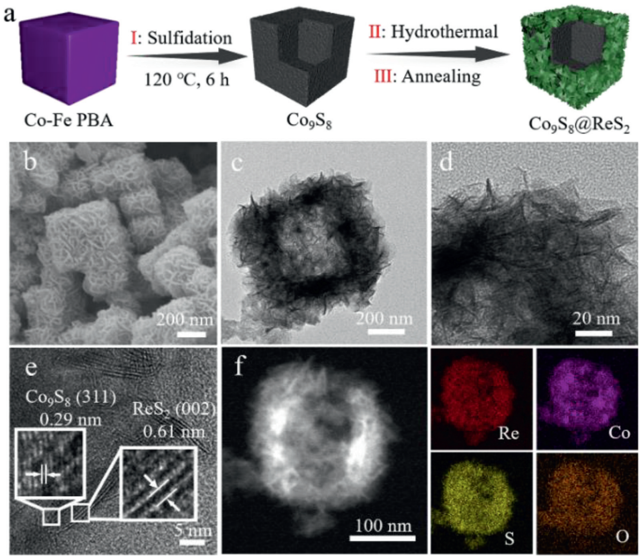

Fig. 1. (a) Schematic illustration for the preparation of core-shell $Co_9S_8@ReS_2$ heterostructure. (b) SEM images of $Co_9S_8@ReS_2$. (c, d) TEM and (e) HRTEM images of $Co_9S_8@ReS_2$. (f) STEM image and elemental mappings of $Co_9S_8@ReS_2$.

The crystal structure of $Co_9S_8@ReS_2$ was analyzed by X-ray diffraction (XRD) in Fig. 2a. The typical diffraction peaks of CoFe PBA are consistent with the PDF card (JCPDS card No. 75-0039) and the sharp peaks indicate high crystallinity (Fig. S3a in Supporting information). In Fig. S3b (Supporting information), the pristine ReS_2 shows characteristic peaks at 14.4°, 32.2°, 34.0° and 57.6° belong to the (002), (020), (200) and $(\bar{4}22)$ planes of triclinic ReS_2 (JCPDS No. 89-0341). The XRD pattern for $Co_9S_8@ReS_2$ shows the co-existence of ReS_2 and Co_9S_8 implying the successful loading of ReS_2 on Co_9S_8 (Fig. 2a). The characteristic peaks at 29.8°, 39.6°, 47.6° and 52.0° correspond to the (311), (331), (511) and (440) planes of Co_9S_8 (JCPDS No. 65-6801), and other peaks is related to the pristine ReS_2. The XRD pattern of $Co_9S_8@ReS_2$ reveals that the 1T phase ReS_2 dominantly exists in $Co_9S_8@ReS_2$ [48].

The surface chemistry and electronic interaction of $Co_9S_8@ReS_2$ were studied by X-ray photoelectron spectroscopy (XPS). The full-scan XPS spectrum indicates that $Co_9S_8@ReS_2$ is composed of Re, Co, S and O elements (Fig. S4a in Supporting information), and all spectra are corrected by C 1s at 284.6 eV (Fig. S4b in Supporting information). The high-resolution Co 2p spectrum can be deconvoluted into two spin-orbit doublets and accompanied satellite peaks. The first doublet at 779.3 eV (Co $2p_{3/2}$) and 794.3 eV (Co $2p_{1/2}$) is assigned to Co^{3+}, and the second doublet at 781.3 eV (Co $2p_{3/2}$) and 797.7 eV (Co $2p_{1/2}$) belongs to Co^{2+}, as well as the corresponding two satellites peaks at 785.0 and 802.9 eV (Fig. 2b), respectively [49]. The Co 2p peaks exhibit high binding energy implying the strong couple of ReS_2 layers with Co_9S_8. For Re 4f spectrum in Fig. 2c, two peaks at 42.1 and 44.5 eV are the indexes to Re $4f_{7/2}$ and Re $4f_{5/2}$, indicating the presence of Re^{4+}. Sulfur species were determined from the high-resolution S 2p spectrum (Fig. 2d). The peaks centering at 162.3 eV and 163.5 eV correspond to the spin-orbital of S $2p_{3/2}$ and S $2p_{1/2}$, and the peak at high binding energy is related to the oxidation state of sulfur, respectively. The total oxygen content of $Co_9S_8@ReS_2$ (19.0%) is lower than that of ReS_2 (21.9%) implying a higher electronic conductivity for $Co_9S_8@ReS_2$, which is favorable for improving the catalytic stability during OER process. All the above characterizations support the successful preparation of the core-shell $Co_9S_8@ReS_2$ heterostructures, and the most possible linkage is the formation of the Co-S-Re bond at the Co_9S_8/ReS_2 interface [50]. The XPS result predicts the strong interaction at the ReS_2/Co_9S_8 interface, which is favorable for improving the electrocatalytic activity of catalysts.

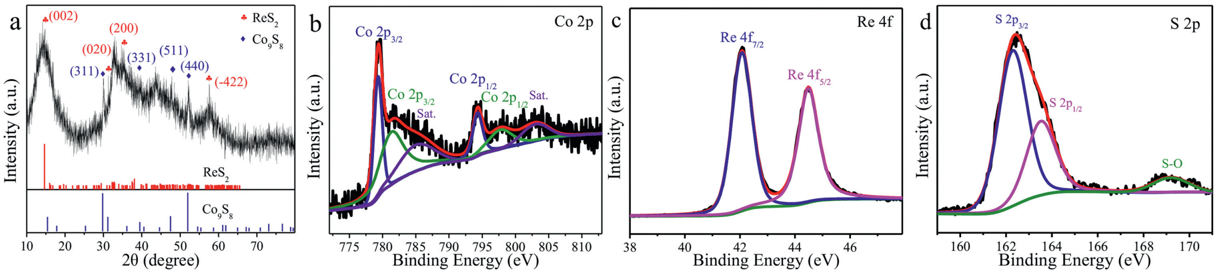

Fig. 2. (a) XRD patterns of $Co_9S_8@ReS_2$. High-resolution XPS spectrum of (b) Co 2p, (c) Re 4f and (d) S 2p for $Co_9S_8@ReS_2$.

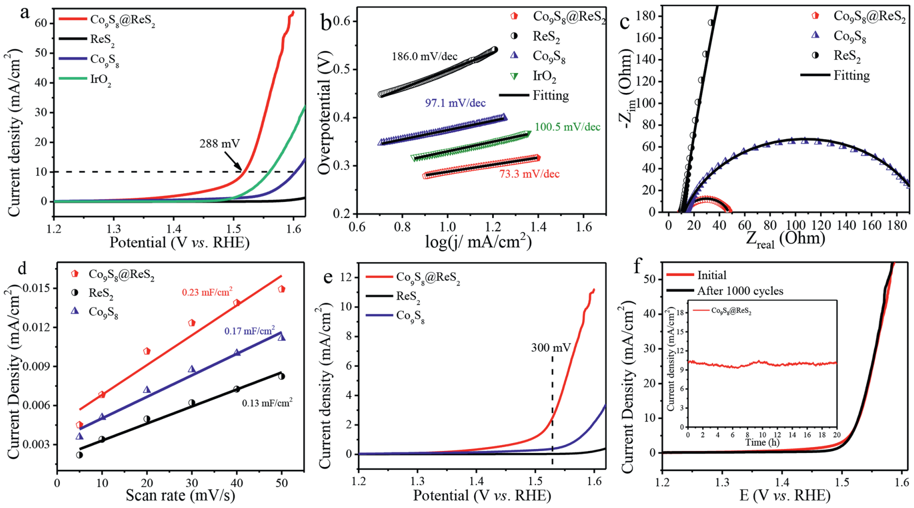

Fig. 3. (a) Polarization curves and (b) Tafel slopes of $Co_9S_8@ReS_2$, Co_9S_8, ReS_2 and IrO_2. (c) Nyquist plots. (d) Linear plot of capacitive current density *vs.* scan rate and (e) specific activity of $Co_9S_8@ReS_2$, Co_9S_8, ReS_2. (f) Polarization curves of $Co_9S_8@ReS_2$ before and after 1000 CV cycles (Inset: Chronoamperometry test for 20 h).

To evaluate the electrocatalytic behaviors of core-shell $Co_9S_8@ReS_2$ heterostructure, the electrolytic oxygen evolution reaction (OER) was measured by a typical three-electrode configuration, and $Co_9S_8@ReS_2$ loading on an inert glassy carbon electrode acts as the working electrode. To manifest the merit of $Co_9S_8@ReS_2$, the pristine ReS_2 and Co_9S_8 were also prepared and evaluated under the same conditions for comparison. Fig. 3a displays the polarization curves after IR correction at a scan rate of 5 mV/s in 1 mol/L KOH. $Co_9S_8@ReS_2$ has an overpotential of 288 mV to deliver the benchmark current density of 10 mA/cm^2, which is smaller than 490 mV for pristine ReS_2, 373 mV for pristine Co_9S_8, 330 mV for the commercial IrO_2 and other reported transition metal sulfides catalysts (Table S1 in Supporting information), respectively. This result is suggested to own better electrocatalytic performance for $Co_9S_8@ReS_2$. Tafel slopes derived from the LSV curves were analyzed to probe the OER kinetics information (Fig. 3b). The value of the Tafel slope for $Co_9S_8@ReS_2$ is 73.3 mV/dec, which is much lower than those of ReS_2 (186.0 mV/dec), Co_9S_8 (97.1 mV/dec) and commercial IrO_2 (100.5 mV/dec), respectively, implying the fast distinct reaction dynamics due to the core-shell nanocubic structure with the vertically aligned surface. Furthermore, the charge transfer kinetics is evaluated by electrochemical impedance spectroscopy (EIS) in Fig. 3c. The EIS data is fitted following a simple Randles equivalent circuit (Fig. S5 and Table S2 in Supporting information), the value of charge transfer resistance (R_{ct}) is 34.8, 187.4 and 1571.0 Ω for $Co_9S_8@ReS_2$, Co_9S_8 and ReS_2. The smaller R_{ct} value implies a faster charge transfer capability during the OER process.

The unique morphology of $Co_9S_8@ReS_2$ can provide abundant ion transport channels and increase the surface area to expose more active sites for OER, which makes $Co_9S_8@ReS_2$ an efficient electrocatalyst with enhanced catalytic activity for water oxidation. The double-layer capacitance (C_{dl}) is obtained by integrating the specific current versus the scan rate from the CV curves in the non-faradic region, and the electrochemically active surface area (ECSA) is determined by C_{dl} (Fig. S6 in Supporting information). The C_{dl} value is calculated to be 0.23 mF/cm^2 for $Co_9S_8@ReS_2$, which is much larger than 0.17 and 0.13 mF/cm^2 for Co_9S_8 and ReS_2 (Fig. 3d), elucidating that the large C_{dl} value for $Co_9S_8@ReS_2$ is favorable for exposing the more active surface to facilitate ion transportation. The specific activity is used to compare the efficiency of catalytic active sites by normalizing the original current to ECSA (Fig. 3e). The specific activity of $Co_9S_8@ReS_2$ is 2.53 mA/cm^2 at an overpotential of 300 mV, which is about 6.66 and 93.70 times higher than that of Co_9S_8 and ReS_2. All these results suggest that the vertically aligned ReS_2 nanosheets on hollow Co_9S_8 nanocubes can increase the number of active sites and further enhance the catalytic OER performance. The catalytic stability is an important criterion for evaluating the performance of electrocatalysts, and the long-term durability of $Co_9S_8@ReS_2$ was evaluated by chronoamperometry (CA) test for 20 h and CV test after 1000 cycles (Fig. 3f). No manifest current density decline is observed after the CA test for 20 h and the applied potential is 1.51 V (*vs.* RHE) in 1 mol/L KOH. Meanwhile, the polarization curve after 1000 CV cycles is almost overlapped with its initial cycle for $Co_9S_8@ReS_2$. The Faradaic efficiency of $Co_9S_8@R4eS_2$ was evaluated by comparing the theoretic and practical amount of oxygen gas produced at 1.51 V for 60 min (Fig. S7 in Supporting information) and the experimental and theoretical data are in good agreement, indicating that the current efficiency of the OER process is close to 100%. All the results reveal that $Co_9S_8@ReS_2$ has outstanding durability for OER in alkaline media.

The morphology and the surface chemical state of $Co_9S_8@ReS_2$ after the CA test were probed by TEM, SEM and XPS in Fig. 4

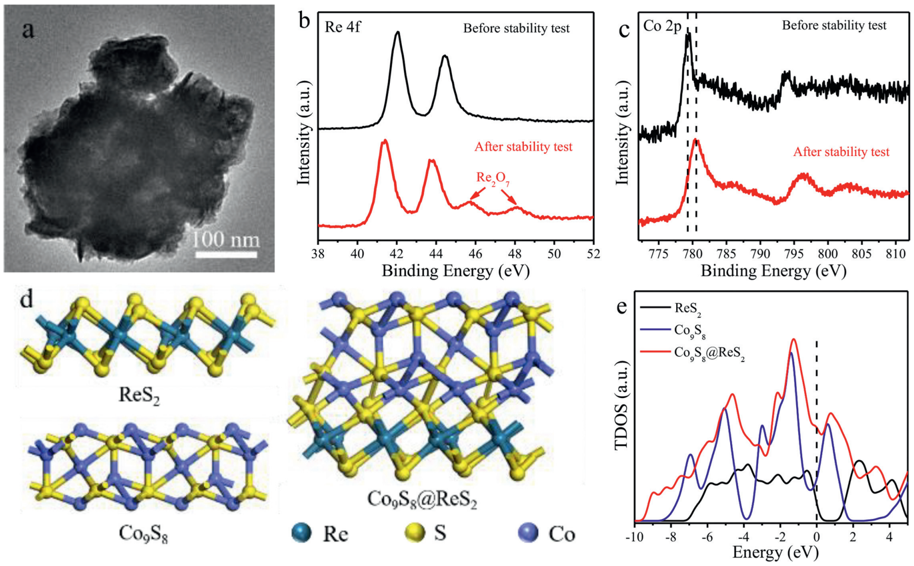

Fig. 4. (a) TEM image of Co_9S_8@ReS_2 after stability test for OER; XPS spectra of (b) Re 4f and (c) Co 2p for Co_9S_8@ReS_2 before and after stability test; (d) The simulated calculation model and (e) the corresponded density of state of ReS_2, Co_9S_8 and Co_9S_8@ReS_2.

and Fig. S8 (Supporting information). The nanocubic morphology remained after the CA test with a rough surface due to the partially oxidized surface (Fig. 4a). The atomic ratio of all elements for Co_9S_8@ReS_2 is listed in Table S3 (Supporting information), and the oxygen content is increased due to the surface oxidation of catalyst. It is found that the Re $4f_{7/2}$ and Re $4f_{5/2}$ peaks shift to a low binding energy direction, and new peaks appear at 45.8 eV and 48.1 eV corresponding to the valence state and bonding transformation from Re-S to Re-O species (Fig. 4b). Fig. 4c shows the Co 2p peaks of Co_9S_8@ReS_2, and the peaks shift to high binding energy after the stability test due to the formation of the Co-O bond. The electronegativity of the S atom is lower than the O atom, and the Metal-O bond is firmed by replacing the S atom with the O atom. The high-resolution O 1s spectrum confirms the formation of a metal-O bong at 529.5 eV (Fig. S8a in Supporting information), which is consistent with the Re 4f and Co 2p spectra. The additional peak of the C-SO_3 bond comes from the residue from the catalyst ink. The metal-S bond shifts to a low binding energy and the SO_x bond species appear at 168.8 eV, which is assigned to the partial surface oxidation of Co_9S_8@ReS_2 with the formation of metal-O and S-O bonds (Fig. S8b in Supporting information).

To further understand the catalytic mechanism of Co_9S_8@ReS_2, the density functional theory (DFT) calculation was carried out. The simulated calculation models of ReS_2, Co_9S_8 and Co_9S_8@ReS_2 could be depicted in Fig. 4d. The density of state (DOS) near the Fermi level is contributed by the d-orbital of Co for Co_9S_8, the contribution of ReS_2 is determined by the 5d orbitals of Re, while the predicted DOS of Co_9S_8@ReS_2 is contributed by the d-orbitals of Co and Re (Fig. S9 in Supporting information), and the formation of heterostructure can improve the D-band contribution near the Fermi level [51,52]. Co_9S_8@ReS_2 shows a higher electronic state than pristine ReS_2 and Co_9S_8 near the Fermi level (Fig. 4e), indicating that the catalytic site was in a highly conductive metallic state [53,54]. The highest electronic state around the Fermi level reveals that the Co_9S_8@ReS_2 heterostructure has higher electronic conductivity and better electrocatalytic OER activity than that of pristine ReS_2 and Co_9S_8, which is matched with the electrochemical results.

In summary, a core-shell Co_9S_8@ReS_2 heterostructure is prepared *via in-situ* growth of ReS_2 nanosheets on the surfaces of hollow Co_9S_8 nanocubes. The core-shell Co_9S_8@ReS_2 heterostructure has excellent catalytic OER performance, such as high stability, rapid charge transfer kinetics, and increased electrochemical surface area. To drive the benchmark current density of 10 mA/cm^2, Co_9S_8@ReS_2 only requires an overpotential of 288 mV with a Tafel slope of 73.3 mV/dec and outstanding long-term stability after chronoamperometry test for 20 h. The high catalytic performance can be attributed to core-shell structure and boosted active sites by hybridizing ReS_2 with Co_9S_8 nanocubes. The current work demonstrates a feasible way for designing the core-shell structured hybrids as efficient catalysts for oxygen evolution reactions.

Declaration of competing interest

The authors declare that they have no known competing financial interests or personal relationships that could have appeared to influence the work reported in this paper.

Acknowledgments

The work is supported by the Natural Science Research of the Jiangsu Higher Education Institutions of China (No. 18KJB150034), Six Talent Peaks Project of Jiangsu Province (No. XCL-103) and 'High-End Talent Project' of Yangzhou University. We also acknowledge the technical support at Testing Center of Yangzhou University.

Supplementary materials

Supplementary material associated with this article can be found, in the online version, at doi:10.1016/j.cclet.2023.108484.

References

[1] H. Luo, Z. Zeng, G. Zeng, et al., Chem. Eng. J. 383 (2020) 123196.
[2] D. Ko, X. Jin, K.-d. Seong, et al., Appl. Catal. B: Environ. 248 (2019) 357–365.
[3] Z.Q. Liu, K. Xiao, Y. Wang, et al., Angew. Chem. Int. Ed. 62 (2023), doi:10.1002/anie.202301408.
[4] W.K. Han, J.X. Wei, K. Xiao, et al., Angew. Chem. Int. Ed. 61 (2022) e202206050.
[5] W.J. Jiang, T. Tang, Y. Zhang, J.S. Hu, Acc. Chem. Res. 53 (2020) 1111–1123.
[6] H. Liu, M. Zha, Z. Liu, et al., Chem. Commun. 56 (2020) 7889–7892.
[7] X. Gu, Z. Liu, M. Li, et al., Appl. Catal. B: Environ. 297 (2021) 120462.
[8] H. Chen, Y. Zhou, W. Guo, B.Y. Xia, Chin. Chem. Lett. 33 (2022) 1831–1840.
[9] Y. Ding, K.W. Cao, J.W. He, et al., Chin. J. Catal. 43 (2022) 1535–1543.
[10] J. Huang, Y. Li, Y. Zhang, et al., Angew. Chem. Int. Ed. 58 (2019) 17458–17464.
[11] L. Li, P. Wang, Q. Shao, X. Huang, Adv. Mater. 33 (2021) 2004243.
[12] K. Xiao, R.T. Lin, J.X. Wei, et al., Nano Res. 15 (2022) 4980–4985.
[13] I.S. Kwon, T.T. Debela, I.H. Kwak, et al., Small 16 (2020) 2000081.
[14] T. Reier, M. Oezaslan, P. Strasser, ACS Catal. 2 (2012) 1765–1772.

[15] Y. Zhao, X. Wang, Z. Li, et al., Chin. Chem. Lett. 33 (2022) 1065–1069.
[16] Q. Shi, C. Zhu, D. Du, Y. Lin, Chem. Soc. Rev. 48 (2019) 3181–3192.
[17] Z. Liu, X. Yang, G. Hu, L. Feng, ACS Sustain, Chem. Eng. 8 (2020) 9136–9144.
[18] Q.L. Hong, B.Q. Miao, T.J. Wang, et al., Energy Lab 1 (2023) 220022.
[19] X. Zou, Y. Wu, Y. Liu, et al., Chem 4 (2018) 1139–1152.
[20] R. Elakkiya, G. Maduraiveeran, Nanoscale 13 (2021) 14837–14846.
[21] Y. Liu, C. Xiao, M. Lyu, et al., Angew. Chem. Int. Ed. 54 (2015) 11231–11235.
[22] T. Liu, P. Li, N. Yao, et al., Adv. Mater. 31 (2019) 1806672.
[23] G. Zhang, Y.S. Feng, W.T. Lu, et al., ACS Catal. 8 (2018) 5431–5441.
[24] W. Zhou, X.J. Wu, X. Cao, et al., Energ. Environ. Sci. 6 (2013) 2921–2924.
[25] X.Y. Yu, L. Yu, H.B. Wu, X.W. Lou, Angew. Chem. Int. Ed. 54 (2015) 5331–5335.
[26] Y. Wang, Y. Wang, L. Zhang, et al., Chem. Asian J. 15 (2020) 2035.
[27] D. Li, C. Liu, W. Ma, et al., Electrochim. Acta 367 (2021) 137492.
[28] C. Xuan, W. Lei, J. Wang, et al., J. Mater. Chem. A 7 (2019) 12350–12357.
[29] Y. Guo, J. Tang, Z. Wang, et al., Nano Energy 47 (2018) 494–502.
[30] X.Y. Yu, Y. Feng, B. Guan, et al., Energ. Environ. Sci. 9 (2016) 1246–1250.
[31] J. Nai, X.W. Lou, Adv. Mater. 31 (2019) 1706825.
[32] L.M. Cao, D. Lu, D.C. Zhong, T.B. Lu, Coord. Chem. Rev. 407 (2020) 213156.
[33] M. Rahman, K. Davey, S.Z. Qiao, Adv. Funct. Mater. 27 (2017) 1606129.
[34] M. Hafeez, L. Gan, A. Saleem Bhatti, T. Zhai, Mater. Chem. Front. 1 (2017) 1917–1932.
[35] Q. Zhang, L. Fu, Chem 5 (2019) 505–525.
[36] J. Xu, C. Fang, Z. Zhu, et al., Nanoscale 12 (2020) 17045–17052.
[37] J. Luxa, P. Marvan, P. Lazar, Z. Sofer, Nanoscale 11 (2019) 14684–14690.
[38] J. Pan, W. Zhang, X. Xu, J. Hu, RSC Adv. 11 (2021) 23055–23063.
[39] Q. Zhang, S. Tan, R.G. Mendes, et al., Adv. Mater. 28 (2016) 2616–2623.
[40] J. Pan, W. Zhang, X. Xu, J. Hu, Phys. Chem. Chem. Phys. 22 (2020) 9415–9423.
[41] Q. Sun, B. Zhang, L. Diao, et al., J. Mater. Chem. A 8 (2020) 11607–11616.
[42] R. Chen, Y. Ao, C. Wang, P. Wang, Chem. Commun. 56 (2020) 8472–8475.
[43] Z. Chen, R. Wu, Y. Liu, et al., Adv. Mater. 30 (2018) 1802011.
[44] X. Yan, L. Tian, M. He, X. Chen, Nano Lett. 15 (2015) 6015–6021.
[45] X.P. Li, L.R. Zheng, S.J. Liu, et al., Chin. Chem. Lett. 33 (2022) 4761–4765.
[46] B. Jiang, Z. Wan, Y. Kang, et al., Nano Energy 81 (2021) 105644.
[47] L. Zhang, J. Rong, Y. Yang, et al., Small (2023), doi:10.1002/smll.202207472.
[48] B. Chen, H. Li, H. Liu, et al., Adv. Energy Mater. 9 (2019) 1901146.
[49] Y. Guo, J. Tang, H. Qian, et al., Chem. Mater. 29 (2017) 5566–5573.
[50] C. Pei, M.C. Kim, Y. Li, et al., Adv. Funct. Mater. 33 (2023) 2210072.
[51] H. Liu, Z. Hu, Q. Liu, et al., J. Mater. Chem. A 8 (2020) 24710–24717.
[52] J. Liu, S. Xiao, L. Chang, et al., J Energy. Chem. 56 (2021) 343–352.
[53] Y. Gu, A. Wu, Y. Jiao, et al., Angew. Chem. Int. Ed. 60 (2021) 6673–6681.
[54] D. Zhao, Z. Li, X. Yu, et al., Chem. Eng. J. 450 (2022) 138254.